minerals

MDPI

Article

Molecular Simulation of Methane Adsorption in Deep Shale Nanopores: Effect of Rock Constituents and Water

Jianfa Wu [1,2], Xuefeng Yang [1,2], Shan Huang [1,2], Shengxian Zhao [1,2], Deliang Zhang [1,2], Jian Zhang [1,2], Chunyu Ren [1,2], Chenglin Zhang [1,2], Rui Jiang [1,2], Dongchen Liu [1,2], Qin Yang [3,4] and Liang Huang [3,4,*]

1 Shale Gas Evaluation and Exploitation Key Laboratory of Sichuan Province, Chengdu 610051, China
2 Shale Gas Research Institute, Southwest Oil & Gas Field Company, PetroChina, Chengdu 610051, China
3 State Key Laboratory of Oil and Gas Reservoir Geology and Exploitation, Chengdu University of Technology, Chengdu 610059, China
4 College of Energy, Chengdu University of Technology, Chengdu 610059, China
* Correspondence: huangliang@cdut.edu.cn

Abstract: The molecular models of nanopores for major rock constituents in deep shale were constructed. The microscopic adsorption behavior of methane was simulated by coupling the grand canonical Monte Carlo and Molecular Dynamics methods and the effect of rock constituents was discussed. Based on the illite and kerogen nanopore models, the discrepancies in microscopic water distribution characteristics were elucidated, the effects of water on methane adsorption and its underlying mechanisms were revealed, and the competitive adsorption characteristics between water and methane were elaborated. The results show a similar trend in the microscopic distribution of methane between different shale rock constituents. Illite and kerogen slit pores have no significant difference in methane adsorption capacity. The adsorption capacity per unit mass of kerogen is greater than that of illite due to the smaller molar mass of the kerogen skeleton and its large intermolecular porosity. Illite has a greater affinity for water than methane. With increasing water content, water molecules preferentially occupy the high-energy adsorption sites and then overspread the entire pore walls to form water adsorption layers. Methane molecules are adsorbed on the water layers, and methane adsorption has little effect on water adsorption. Kerogen is characterized as mix-wetting. Water molecules are preferentially adsorbed on polar functional groups and gather around to form water clusters. In kerogen with high water content, methane adsorption can facilitate water cluster fusion and suppress water spreading along pore walls. In addition to adsorption, some water molecules dissolve in the kerogen matrix.

Keywords: deep shale gas; rock constituent; kerogen; adsorption; water; molecular simulation

Citation: Wu, J.; Yang, X.; Huang, S.; Zhao, S.; Zhang, D.; Zhang, J.; Ren, C.; Zhang, C.; Jiang, R.; Liu, D.; et al. Molecular Simulation of Methane Adsorption in Deep Shale Nanopores: Effect of Rock Constituents and Water. *Minerals* **2023**, *13*, 756. https://doi.org/10.3390/min13060756

Academic Editor: Luca Aldega

Received: 5 May 2023
Revised: 25 May 2023
Accepted: 29 May 2023
Published: 31 May 2023

1. Introduction

The Sichuan Basin in China has abundant shale gas reserves, wherein the gas reserves of deep shale with the depth ranging between 3500 and 4500 m can be up to 8.7×10^{12} m^3, accounting for 87% of the total reserves for shale shallower than 4500 m [1]. Deep shale gas has become the major field for increasing shale gas production and reserves. Deep shale gas reservoirs, with temperatures up to 150 °C and pressure exceeding 90 MPa, are greatly different from middle-deep shale gas reservoirs in mineral constitutes, pore structures, and fluid occurrence characteristics [2]. The understanding of the microscopic occurrence characteristics of deep shale gas is significant to the evaluation of shale gas reserves and the interpretation of gas production performances.

Deep shale possesses complex rock constituents, including various inorganic minerals (e.g., detrital minerals, carbonate minerals, and clay minerals) and organic matter (e.g., kerogen, asphaltene, and resin) [3,4]. In the actual deep shale gas reservoir, organic matter is dispersed in the inorganic minerals. Shale gas reservoirs are rich in nanoscale pores and throats, and the average pore size is only a few nanometers [5–7]. Shale gas in nanoscale

pore structure is stored as adsorbed gas, free gas, and dissolved gas, in which adsorbed gas may account for 20%–85% [8]. The proportion of adsorbed gas in deep shales is lower than in medium-deep shales, but adsorbed gas remains one of the dominant forms of deep shale gas. Organic matter and clay minerals in shales are deemed as the major media for adsorbed gas due to their abundant nanopores and large specific surface area [9]. Similar to rock constituents, shale gas is mixed with multi-components, wherein methane is the most dominant component [10]. Some scholars compared the methane adsorption capacity in different shale media [11–15]. Heller and Zoback [11] measured methane adsorption on pure carbon, illite, and kaolinite samples. Pure carbon has the greatest adsorption capacity, and illite has a greater adsorption capacity than kaolinite. Tian et al. [12] detected similar methane adsorption capacity between illite, montmorillonite, and kaolinite using molecular simulation. Onawole et al. [13] found stronger adsorption of methane on the kaolinite region compared with the silica region in a combined silica-kaolinite surface through molecular simulation. Bakshi and Vishal [14] summarized the dependence of methane adsorption capacity on organic pore characteristics, including total organic content, kerogen type, and thermal maturity. Huang et al. [15] concluded using molecular simulation that methane adsorption capacity is in the order of type I < type II < type III for different organic types. To date, the comparisons of methane adsorption capacity in different shale constitutes have been mainly performed in moderate temperature and pressure conditions, and no consistent conclusions have been reached. To the best of our knowledge, the discrepancies of methane adsorption in various rock constituents of deep shale in high-temperature and high-pressure conditions have not been reported.

Ultra-low water saturation is characteristic of shale gas reservoirs [16]. Owing to the differences in wettability, organic matter, and clay minerals in shales show different features of water distribution. Previous studies of microscopic water distribution in minerals [17,18] and organic matter [15,19] have demonstrated the strong hydrophilicity of clay minerals and the mixed wettability of organic matter. Extensive experiments [20,21] and molecular simulations [18,22] have shown that water can significantly reduce the methane adsorption capacity in shale pores, with mechanisms including adsorption site capture, pore space occupation, and methane partial pressure reduction [15,19,23]. Previous studies of methane adsorption in water-bearing shale pores have mainly focused on the influence of water on methane adsorption and its mechanisms. The effect of methane adsorption on water distribution in different shale media in high temperature and pressure conditions remains to be clarified. In addition, the competitive adsorption characteristics between methane and water in shale nanopores in deep reservoir conditions have not been elucidated.

This work focuses on the deep shales of the Longmaxi Formation with a depth larger than 4000 m in Luzhou Block, southern Sichuan Basin. The representative mineral models in shale were constructed based on shale mineral composition analysis, and the kerogen models were built based on the previously established structural unit of kerogen. The molecular simulation method was used to simulate the adsorption behavior of methane under high temperatures and pressure in deep shale. The discrepancies of methane adsorption in different shale rock constitutes were clarified, the differences in microscopic water distribution in shale illite and kerogen pores were elucidated, and the microscopic competitive adsorption characteristics between methane and water were elaborated. The results of this work can enrich the occurrence theory of deep shale gas, facilitating gas reserve evaluation and resource exploitation.

2. Methodology of Molecular Simulation

2.1. Molecular Models of Various Shale Constituents

Shale samples were acquired from Longmaxi Formation with a depth larger than 4000 m in Luzhou Block, southern Sichuan Basin. Table 1 lists the mineral compositions of studied shales, which include detrital minerals, carbonate minerals, and clay minerals. Detrital minerals mainly consist of quartz and feldspar; carbonate minerals mainly consist of calcite and dolomite, and clay minerals mainly consist of illite and chlorite. Molecular

models of the major shale minerals were established to investigate the effect of mineral constituents.

Table 1. Mineral compositions of studied deep shales.

Sample	Mineral Composition/w.t.%						
	Quartz	Feldspar	Calcite	Dolomite	Illite	Chlorite	Others
S1	81.27	4.57	1.03	3.24	3.54	2.51	3.83
S2	63.27	8.41	6.64	6.19	7.67	2.65	5.16
S3	56.19	4.87	12.68	9.88	6.49	4.42	5.46
S4	74.48	6.05	3.39	3.83	4.13	1.92	6.19
S5	47.35	13.42	2.21	1.77	23.89	6.19	5.16
S6	29.20	9.88	6.19	7.08	36.58	6.64	4.42
S7	26.70	12.39	3.24	6.49	38.94	7.08	5.16
S8	25.07	10.03	9.73	3.98	40.27	5.60	5.31

The unit cell structures of quartz, albite, calcite, dolomite, and chlorite in the mineral models were derived from the database of the Materials Studio package. The unit cell structure of illite was established by Geatches and Wilcox [24]. The unit cell parameters of each model are listed in Table 2. Wherein the molecular formulas of quartz, albite, calcite, dolomite, illite, and chlorite are SiO_2, $NaAlSi_3O_8$, $CaCO_3$, $CaMg(CO_3)_2$, $K(Si_7Al)Al_4O_{20}(OH_4)$, and $Mg_4FeAl[AlSi_3O_{10}](OH)_8$, respectively.

Table 2. Unit cell parameters of shale mineral models.

Mineral Model	Unit Cell Parameter					
	a/Å	b/Å	c/Å	α/°	β/°	γ/°
Quartz	4.91	4.91	5.40	90.00	90.00	120.00
Albite	8.12	12.76	7.16	94.22	116.80	87.71
Calcite	4.99	4.99	17.06	90.00	90.00	120.00
Dolomite	4.81	4.81	16.01	90.00	90.00	120.00
Illite	5.22	9.00	10.32	90.26	103.05	89.97
Chlorite	5.22	9.06	28.38	90.00	93.67	90.00

The molecular models of various minerals with slit-shaped nanopores are presented in Figure 1. Supercells were initially constructed by expanding the unicellular structure in the x, y, and z directions. Subsequently, pore walls were generated along the cleavage planes of each mineral and then assembled to form the nanopore models. The relatively stable mineral cleavage plane was selected as the slit wall surface, which was (001) cleavage plane for quartz, albite, illite, and chlorite models and (104) cleavage plane for calcite and dolomite models. Each mineral model was designed with an equal pore diameter (6 nm), and the wall thickness was set to be larger than the cutoff radius in the simulation. To mitigate the influence of the periodic boundary condition in the normal direction of the slit, a vacuum space (2 nm) was set outside the pore walls.

In addition to inorganic minerals, shale also contains a certain amount of organic matter. Based on the molecular structure of kerogen in the studied shales, the kerogen slit model was established using the excision method, as detailed in Ref. [1]. To clarify the adsorption discrepancies between inorganic minerals and organic matter in shale, the adsorption characteristics of methane and water in kerogen and illite nanopore models were compared.

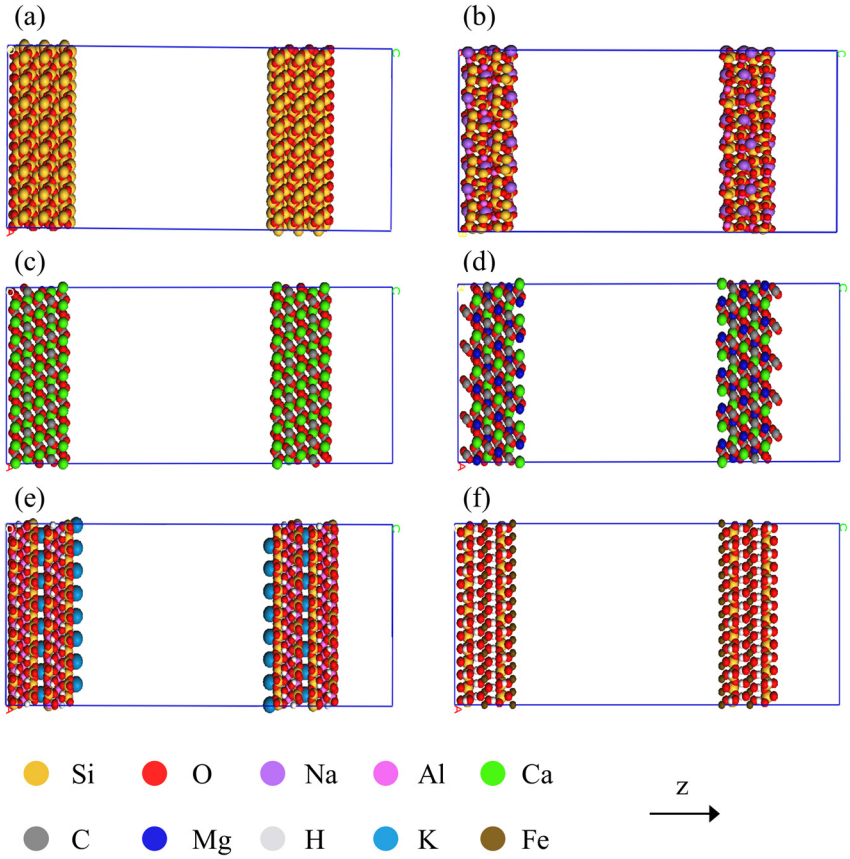

Figure 1. Molecular models of slit nanopores in various shale minerals: (**a**) Quartz; (**b**) Albite; (**c**) Calcite; (**d**) Dolomite; (**e**) Illite; (**f**) Chlorite.

2.2. Simulation Detail of Gas–Water Adsorption

The molecular simulator, LAMMPS [25], was used for the simulation of methane and water adsorption. The water-bearing models were created by inserting a certain number of water molecules into the nanopores through grand canonical Monte Carlo (GCMC) simulation, and the inserted water molecules were then equilibrated using molecular dynamics (MD) simulation. The number of inserted water molecules is determined by the number of GCMC steps. Subsequently, the adsorption equilibrium of methane in the nanopores was simulated by the coupling of grand canonical Monte Carlo and molecular dynamics (GCMC-MD) algorithms. During the coupling GCMC-MD simulation, the insertion/deletion of methane was performed by the GCMC algorithm, and the relaxation of methane, as well as water molecules, was performed by the MD algorithm. Among the mineral components in shales, the molecular models of quartz, feldspar, illite, and chlorite were described using the ClayFF force field [26]; the molecular models of calcite and dolomite were described using the force field fitted by Xiao et al. [27], in which the force field parameters for Mg in dolomite were described using the ClayFF force field. The molecular models of kerogen were described using the CVFF force field [28]. Methane and water were described using the TraPPE united-atom force field [29] and SPC/E force field [30], respectively. The non-bonded interaction between different atoms was characterized using the LJ 12-6 potential function and the Coulomb potential. The long-range electrostatic interaction was described by the Ewald summation [31]. The non-bonded parameters for unlike atoms were obtained using the Lorentz–Berthelot combining rules [32].

The simulation was performed in the canonical ensemble, and the temperature was regulated using the Nosé–Hoover algorithm [33]. The nanopore structure was fixed during the simulation. Periodic boundary conditions were used in the x, y, and z directions, and the cutoff radius in the simulation is 14 Å. The simulation time for water equilibrium is up

to 10 ns with a timestep of 1 fs. Upon water equilibrium, the water content was determined by the void volume of nanopores reduced by water,

$$S_w = \frac{V_p^d - V_p^w}{V_p^d} \times 100\ \% \quad (1)$$

where S_w is the water content of the model, V_p^d is the pore space in the dry model, V_p^w is the void space in the water-bearing model. V_p^d and V_p^w were calculated using the Metropolis Monte Carlo integration method [34], wherein the probe size was set to be the dynamic diameter of methane.

The coupling GCMC-MD algorithm for methane adsorption simulation was performed through the loop iteration of 10,000 MD steps and 2500 GCMC steps until the temperature, energy, and methane loading achieved equilibrium. The system pressure in methane adsorption was determined using the input chemical potential. The correlation between chemical potential and pressure was constructed in our previous work [35],

$$\mu = 0.78692 \times \ln P - 0.02354 \times T - 7.45195 \quad (2)$$

where μ is the chemical potential; P is the system pressure; T is the system temperature.

Upon adsorption equilibrium, the number of methane molecules in the nanopore was ensemble-averaged to determine the total gas amount, the standard error of which was smaller than 5%. The total gas amount can be converted into the excess adsorption amount,

$$n_e = n_t - \rho V_p \quad (3)$$

where n_e is the excess adsorption amount; n_t is the total gas amount; ρ is the bulk gas density; V_p is the void space in the model derived using the methane probe.

The validation of the force field and the simulation settings is the prerequisite for subsequent simulations. The validations of the chosen force field and simulation settings have been reported in our previous work [35]. Under the given temperature and chemical potential, the simulated pressure matches well with the targeted value, and the simulated density is in good agreement with the National Institute of Standards and Technology (NIST) database.

3. Effects of Shale Constituents

3.1. Differences between Inorganic Mineral Compositions

Figure 2 shows the methane gas amount in different shale mineral models. The order of the methane gas amount between the mineral models varies for different units of methane gas amount. The methane gas amount, expressed per unit mass of mineral, is related to the pore wall thickness. As the pore wall thickness increases, the specific surface area per unit mass of the mineral decreases, thus reducing the adsorption capacity of the mineral. By contrast, the methane gas amount, expressed per surface area of mineral, is not affected by the pore wall thickness once the pore wall thickness is larger than the cutoff radius in the simulation. In this work, the adsorption capacity of mineral models with the same pore size was compared at a molecular scale, which can be properly described with the methane gas amount per unit of mineral area.

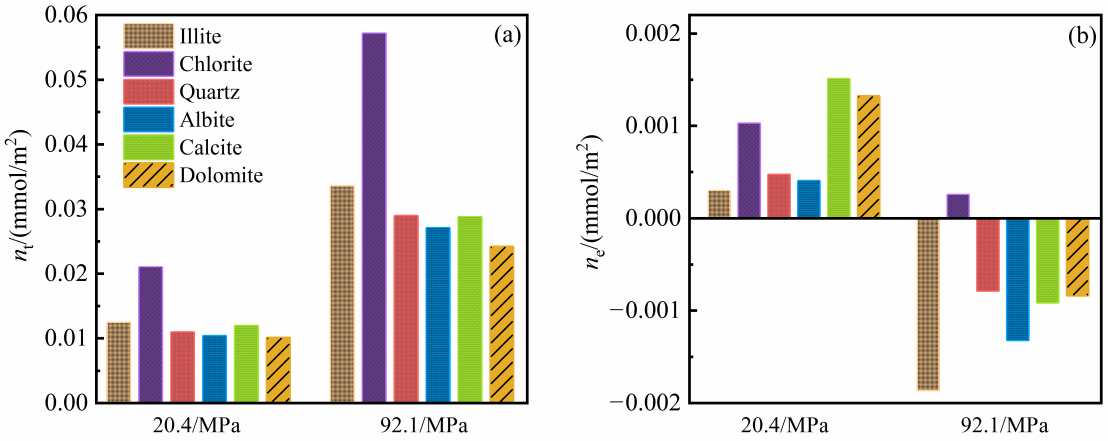

Figure 2. Methane amount in different shale minerals (150 °C): (**a**) Total gas amount; (**b**) Excess adsorption amount.

Figure 2a shows a consistent mineral order of total gas amount at both shallow-zone low pressure (20.4 MPa) and deep-zone high pressure (92.1 MPa). The total gas amount is largest in chlorite, followed by illite, and is basically consistent in carbonate minerals and detrital minerals. The total methane amount at 20.4 MPa is 0.021 mmol/m^2 in chlorite, 0.010 mmol/m^2 in albite, and 0.010 mmol/m^2 in dolomite. As pressure increases to 92.1 MPa, the total methane amount rises to 0.057 mmol/m^2, 0.027 mmol/m^2, and 0.024 mmol/m^2 in chlorite, albite, and dolomite, respectively. At low pressure in the shallow zone and high pressure in the deep zone, the total amount of methane in chlorite is twice that in albite and dolomite. The total methane amount is dependent on the pore volume per unit mineral area (specific pore volume), and the mineral order of total methane amount is basically consistent with the mineral order of specific pore volume (Table 3). The simulation results of the regular slit-shaped pores in minerals at a molecular level may differ from the mineral order of adsorption capacity in subsurface shale reservoirs, which is governed by multiple factors such as the specific surface area of minerals, surface chemistry, and pore structure. Compared to low pressure, the total methane amount is higher in high pressure. As pressure rises, both the free gas density in the nanopore and the adsorbed gas density on the pore surface increase (Figure 3), leading to the increasing total gas amount.

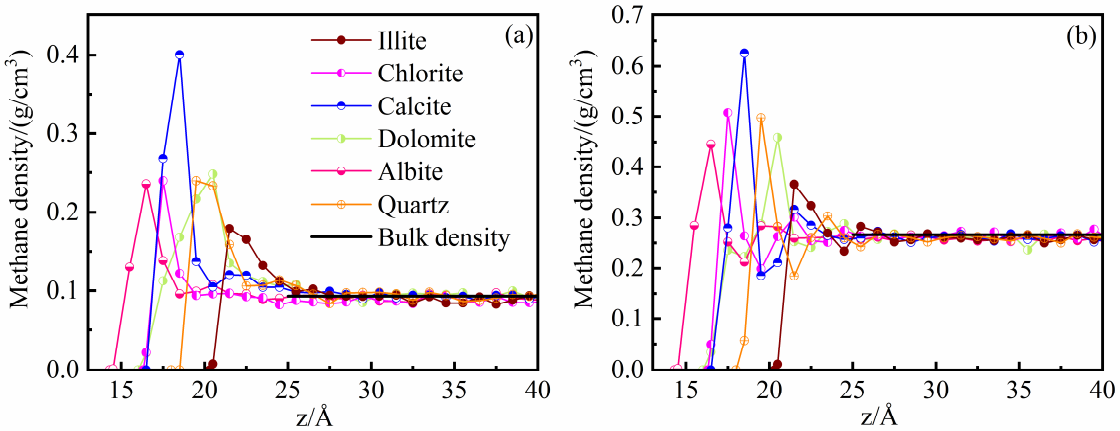

Figure 3. Methane density profile in the slit of different shale minerals (150 °C): (**a**) 20.4 MPa; (**b**) 92.1 MPa.

Table 3. Pore structure parameters of shale mineral models.

Mineral Model	Skeleton Molecular Weight/ (g/mol)	Accessible Surface Area/ (10^{-20} m^2)	Accessible Pore Volume/ (10^{-30} m^3)	Specific Surface Area/ (m^2/g)	Specific Pore Volume/ (10^{-10} m)
Illite	97,024	4155	87,370	257.8	21.0
Chlorite	89,208	2018	70,033	136.2	34.7
Quartz	70,464	4030	73,099	344.3	18.1
Albite	100,608	7902	136,880	472.8	17.3
Calcite	85,520	4867	88,119	342.7	18.1
Dolomite	79,240	5550	84,738	421.7	15.3

Figure 2b shows positive excess adsorption amounts of methane in minerals at 20.4 MPa, which is largest in calcite and smallest in illite. At 92.1 MPa, the excess adsorption of all minerals except chlorite is negative. The excess adsorption of illite is the smallest. The excess adsorption amount of methane is jointly dominated by the adsorbed gas amount on the pore surface and free gas density in pores. Figure 3 shows the methane density profiles in the slits of different minerals. The simulated methane density at the pore center matches well with the bulk methane density, which validates the force field and simulation settings. The mineral order of the adsorbed phase peak density on the pore walls is similar at 20.4 MPa and 92.1 MPa; calcite shows the largest density and illite shows the smallest. Despite the discrepancies in methane adsorption capacity between different minerals, the microscopic adsorption characteristics of methane in the mineral nanopores are basically consistent. At shallow-zone low pressure, methane is adsorbed in a single layer on the pore wall of each mineral, and the adsorption phase density has a certain correlation with the excess adsorption amount. Excess adsorption is defined as the absolute adsorption minus the amount of free gas that can be stored in the adsorption volume. The free gas density is consistent among the minerals in the same temperature and pressure conditions. Thus, the excess adsorption is mainly affected by the adsorption density and adsorption volume. At deep-zone high pressure, a concavo-convex transition zone occurs near the adsorption layer on the pore walls, which affects the adsorption volume of methane. Consequently, the excess adsorption at high pressure (Figure 2b) presents no pronounced correlation with the corresponding adsorption density (Figure 3b). The concavo-convex transition zone may be attributed to the disordered molecular arrangement in the adsorption layer, the attraction of methane molecules in the transition zone by pore walls, and the repulsion of methane molecules in the transition zone by the molecules in the adsorption layer.

3.2. Discrepancies between Illite and Kerogen

The adsorbed state of shale gas is mainly stored in the organic matter and clay minerals owing to their abundant nanopores and huge specific surface areas. Illite is the most common clay mineral in shale reservoirs, and it can capture the typical microscopic distribution trend of methane among different mineral pores (Figure 3). Thus, illite can be a representative mineral for the comparison of adsorption characteristics and mechanisms with kerogen. The adsorption data in shale kerogen [1] and shale illite [35] is integrated to compare the adsorption discrepancies between shale kerogen and illite toward methane. Figure 4 shows the methane amount in the nanopore of shale kerogens and illite. Different from the illite model with a slit-shaped pore, the kerogen model contains both a slit-shaped pore and numerous inter-molecule pores. Owing to the differences in pore structures, the discrepancies in adsorption capacities between kerogen and illite are properly described by the methane amount per unit mass of adsorbents. As shown in Figure 4, kerogen and illite pores present similar adsorption characteristics toward methane. The total gas amount monotonically increases with pressure. Although the increase is smaller under high pressure, the total gas amount is still not saturated under 90 MPa. According to Figure 3,

the increased total gas amount is composed of free gas in the middle of the pore and the adsorbed gas on the pore surface. At high pressure, the increase in free and adsorbed gas density decreases, causing the increase in the total gas amount to decrease. The excess adsorption amount of methane increases first and then decreases with increasing pressure, reaching the maximum at about 20 MPa. The difference between the free and adsorbed gas densities peaks at the excess adsorption maximum. The total gas amount and excess adsorption amount are greater in the kerogen model compared to the illite model. The total gas amount in kerogen is 7.14 mmol/g at 90 MPa, which is over 2 times the total gas amount in illite (2.52 mmol/g). The excess adsorption maximum (1.68 mmol/g) in kerogen is 5 times that in illite (0.33 mmol/g).

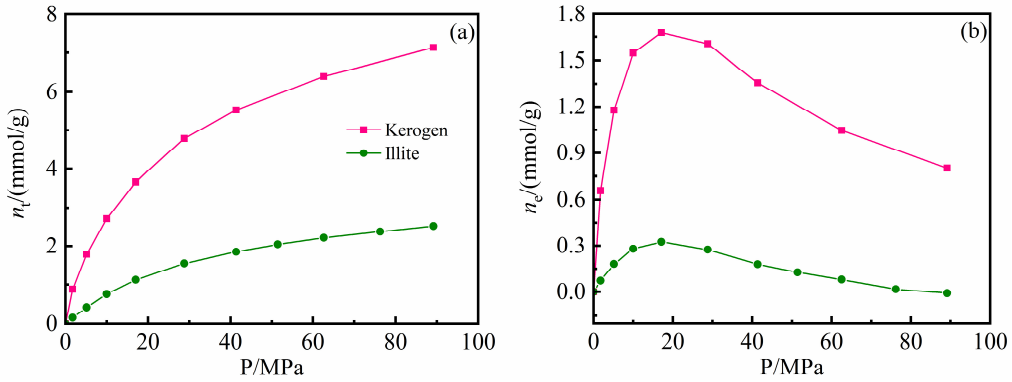

Figure 4. Methane amount in the nanopores of shale kerogen [1] and illite [35] (120 °C): (**a**) Total gas amount; (**b**) Excess adsorption amount.

Figure 5 shows similar trends and values for the peak density of the methane adsorption phase on the slit pore walls in the illite and kerogen models. The peak density of the methane adsorbed phase was averaged from the two adsorption peaks on the two slit surfaces based on the methane density profile. The methane density profile was determined by averaging the last 500 snapshots, and the standard error was less than 3%. The peak density increases with pressure, but the rate of increase becomes small at high pressure. At pressures higher than 20 MPa, the peak density of the adsorbed phase on the kerogen slit surfaces is slightly lower than that on the illite slit surfaces, resulting in a greater decrease in the excess adsorption amount in the kerogen pores at high pressure. Figure 5 shows that kerogen and illite slit pores do not differ significantly in terms of their intrinsic adsorption capacity for methane. The higher adsorption capacity of kerogen than illite shown in Figure 4 can be attributed to the lower molar mass and large intermolecular porosity of the kerogen skeleton. The intermolecular pores, which are mainly ultra-micropores with pore diameters <0.7 nm, have large specific surface areas and could provide abundant adsorption sites in the kerogen model.

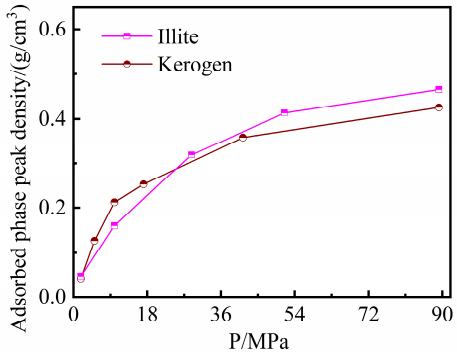

Figure 5. Peak density of the methane adsorbed phase on the slit surfaces of shale kerogen [1] and illite [35] (120 °C).

4. Effects of Water in Shale Nanopores

4.1. Microscopic Distribution of Water

The microscopic distribution of water in the shale illite and kerogen models was performed by MD simulation at 120 °C. Three water-bearing illite models were established based on the common water distribution patterns in clay mineral pores. Figure 6 shows the microscopic distribution of water molecules in illite nanopores. The water content of 7.17% corresponds to an unsaturated state of monolayer adsorption on the slit-shaped pore wall; the water content of 29.53% corresponds to a nearly saturated state of monolayer adsorption; and the water content of 63.54% corresponds to an over-saturated state of monolayer adsorption. Water molecules are mainly adsorbed on the high-energy sites of the slit wall at a water content of 7.17%. Numerous high-energy adsorption sites remain unoccupied on the wall since the adsorption layer is not saturated. As the water content rises to 29.53%, the thickness of the water adsorption layer increases. The high-energy sites on the wall are basically filled by the water molecules, and part of the water molecules accumulate on the water adsorption layer. At the water content of 63.54%, the high-energy adsorption sites on the wall surface are completely occupied. The excess water molecules are adsorbed on the water adsorption layer, blocking part of the slit pore space. The microscopic distribution characteristics of water in the illite pores confirm the strong hydrophilic nature of illite. At low water contents (Figure 6a,b), water molecules are preferentially adsorbed on the illite surfaces due to the strong attraction interaction.

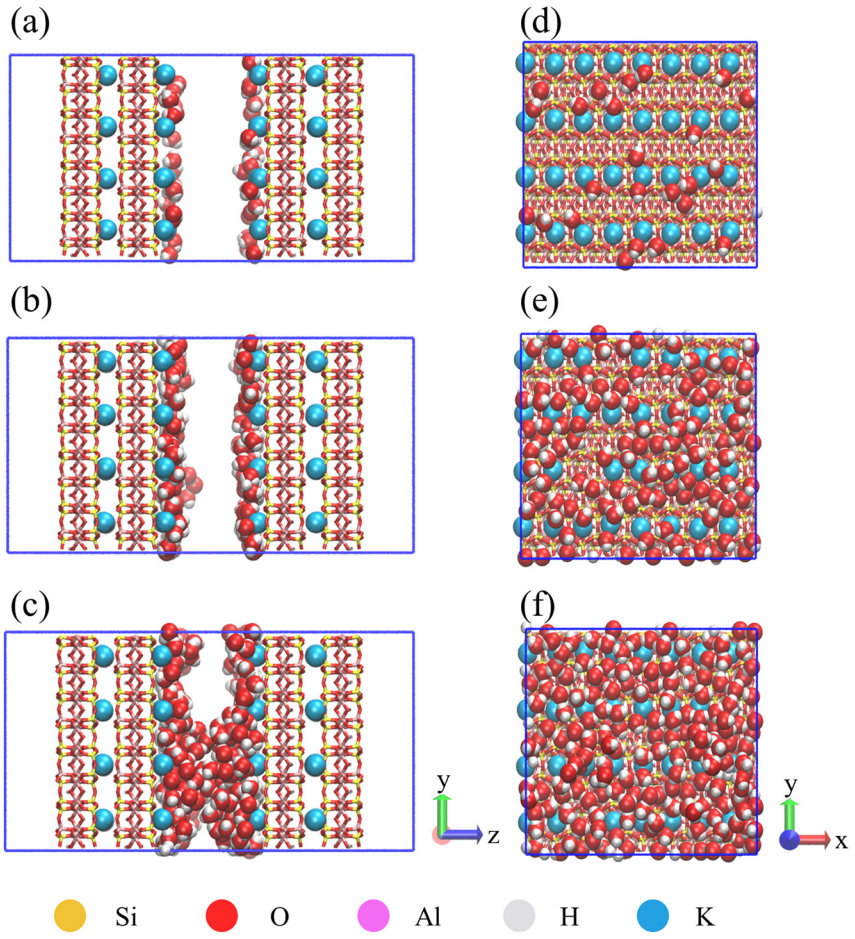

Figure 6. Water distribution in illite nanopores (2 nm): (**a**) Water content of 7.17% (side view); (**b**) Water content of 29.53% (side view); (**c**) Water content of 63.54% (side view); (**d**) Water content of 7.17% (top view of pore wall); (**e**) Water content of 29.53% (top view of pore wall); (**f**) Water content of 63.54% (top view of pore wall).

Figure 7 presents the microscopic distribution of water molecules in kerogen nanopores. At the low water content (11.10%), water molecules are adsorbed and accumulated near the polar functional groups on the slit wall. With the increase in water content, the cluster structure of water molecules enlarges, and a small amount of water molecules are dissolved in the kerogen matrix. At the higher water content (32.23%), the small water clusters are attracted to the large water clusters, merging into a larger molecular cluster. At the high water content (64.28%), most of the pore space in the kerogen model is occupied by the water molecules. Different from the illite model, the microscopic distribution characteristics of water in the kerogen pores indicate a mixed wettability of kerogen.

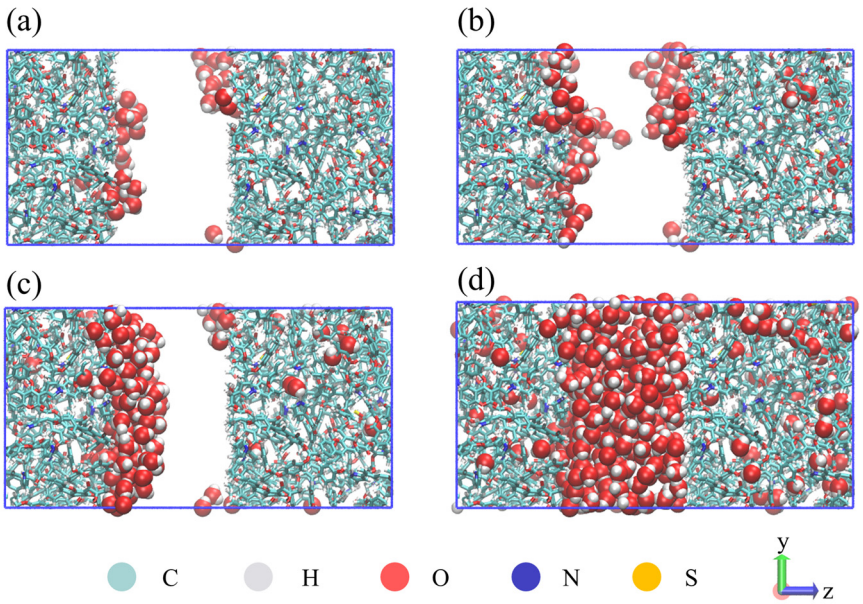

Figure 7. Water distribution in kerogen nanopores (2 nm): (**a**) Water content of 11.10% (side view); (**b**) Water content of 12.17% (side view); (**c**) Water content of 32.23% (side view); (**d**) Water content of 64.28% (side view).

4.2. Water Effects on Methane Amount

As shown in Figures 6 and 7, water can reduce the effective pore space for methane storage and occupy the high-energy sites for methane adsorption, thus affecting the occurrence behavior of methane. Figure 8 shows the amount of methane in the illite models under different water contents. The pressure in Figure 8 refers to the system pressure for methane adsorption in the water-bearing models. With the increase in water content, the total gas amount and excess adsorption amount of methane in the illite pores decrease monotonously. Compared with the dry illite pores, the total methane amount decreases by 50.8% and the maximum excess adsorption decreases by 60.6% in the illite pores with a water content of 63.54%. As the water content increases, the slope of the ascending portion of the excess adsorption curve decreases and the adsorption rate decreases, indicating water molecules gradually occupy the high-energy adsorption sites on the illite surfaces. At the water content of 63.54%, the pressure corresponding to the maximum excess adsorption decreases and the coverage of the water layer on the illite surfaces reduces the affinity of the illite pores for methane. As the water adsorption layer occupies part of the pore volume, the calculation of methane content in the water-bearing pores needs the correction of the effective pore volume. Figure 8 shows that the pore volume without the correction of the water effect greatly underestimates the excess adsorption of methane, and its effect increases with increasing pressure.

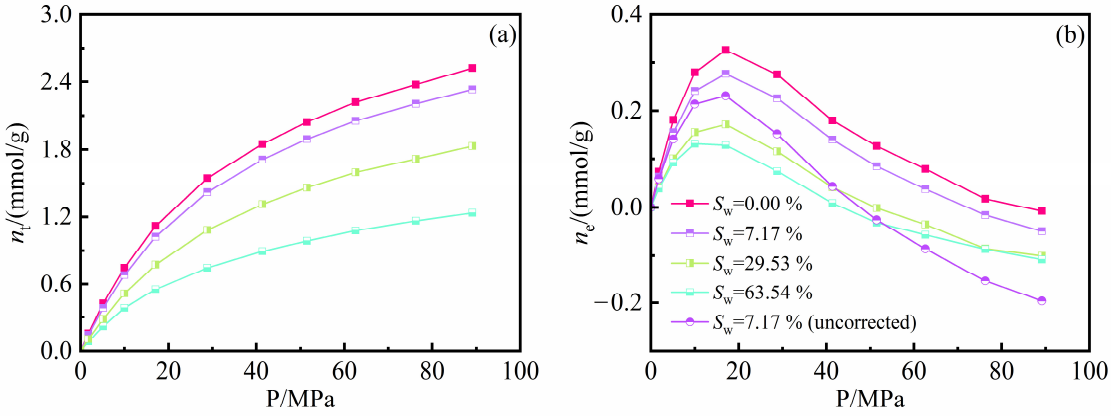

Figure 8. Methane amount in illite nanopores with different water contents (S_w) (120 °C): (**a**) Total gas amount; (**b**) Excess adsorption amount.

Figure 9 shows the methane amount in the kerogen models under different water contents. The total methane amount decreases with increasing water content at 17.1 MPa and 89.2 MPa because water molecules gradually occupy the effective pore space in kerogen (Figure 7). As the water content in the dry model increases to 32.23%, the total gas amount decreases by 27.9% at 17.1 MPa and 28.7% at 89.2 MPa. The excess adsorption amount of methane decreases with increasing water content at 17.1 MPa. At 89.2 MPa, the excess adsorption amount in the water-bearing kerogen is lower than that in the dry kerogen, but the excess adsorption difference between different water contents is not significant. Different from the spread of water molecules on the illite surfaces, water molecules on the kerogen surfaces are preferentially accumulated into a water cluster structure. The water cluster expands gradually with increasing water content, which can exert a larger influence on the effective pore space than on methane adsorption.

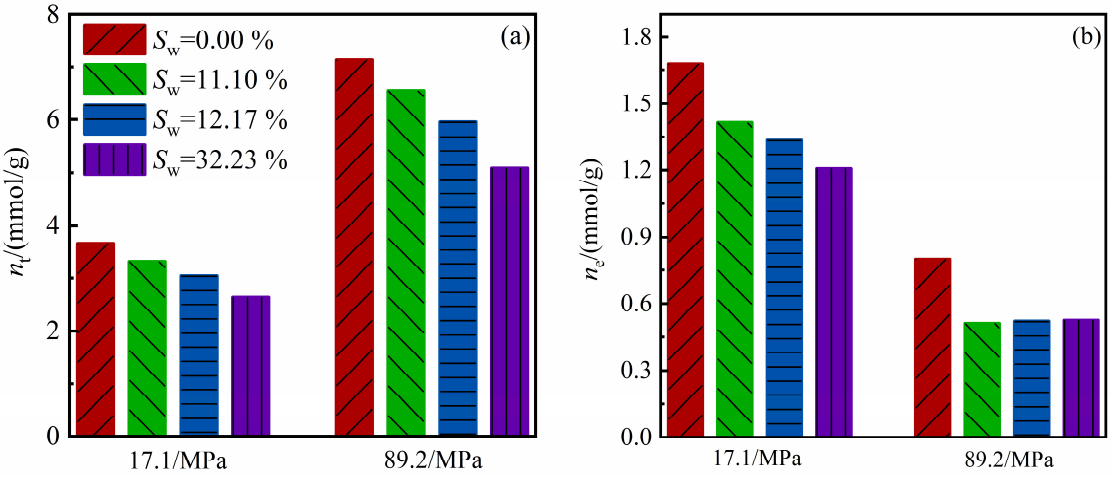

Figure 9. Methane amount in the kerogen models with different water contents (120 °C): (**a**) Total gas amount; (**b**) Excess adsorption amount.

4.3. Competitive Adsorption between Water and Methane

In order to study the effect of methane adsorption on water distribution in water-bearing pores, the water density profiles in the illite and kerogen pores before and after methane adsorption were compared (Figure 10). As seen from Figure 10a, water molecules are preferentially adsorbed on the pore walls of illite before methane adsorption. The adsorption layer density of water molecules gradually increases with increasing water content. At the water content of 63.54%, the water adsorption layer is over-saturated, and part of the water molecules escape to the middle pore spaces. By comparing the water

density profiles before and after methane adsorption (Figure 10a,b), methane adsorption is observed to have little effect on water distribution in illite. This indicates that illite is strongly hydrophilic and the interaction of pore walls with water molecules is greater than that with methane molecules. Methane molecules cannot replace water molecules preferentially adsorbed on the illite walls.

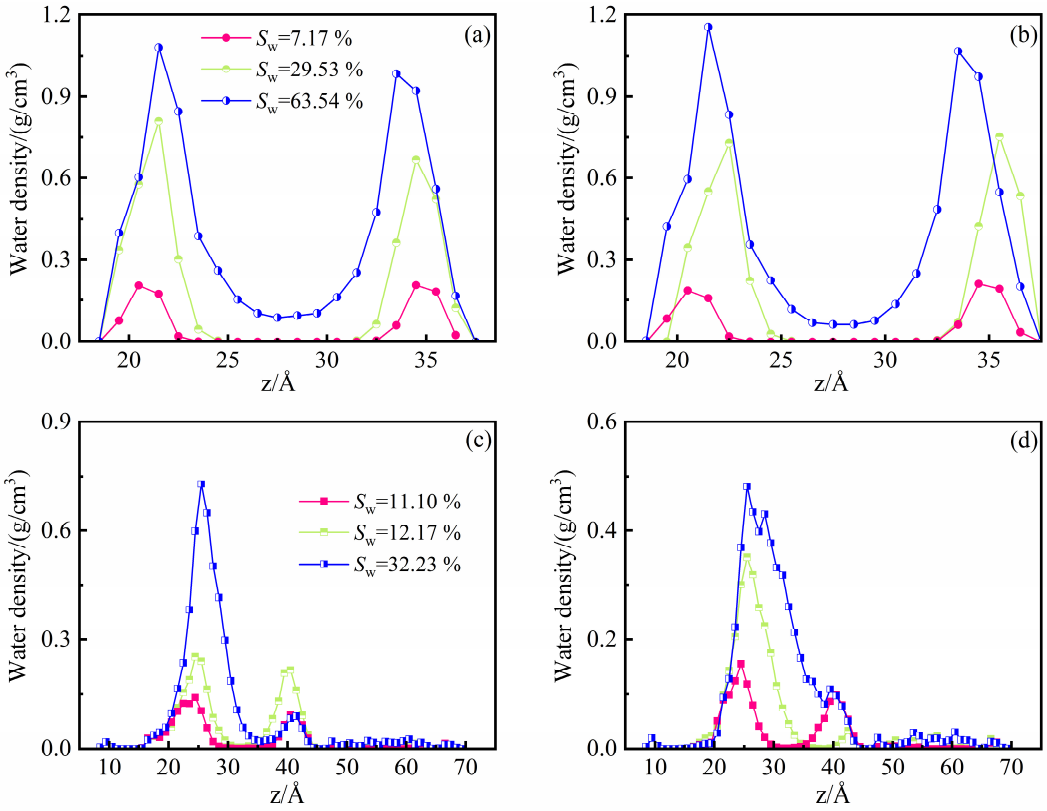

Figure 10. Water density profiles in shale nanopores before and after methane adsorption (120 °C): (**a**) Before methane adsorption in illite; (**b**) After methane adsorption in illite (89.2 MPa); (**c**) Before methane adsorption in kerogen; (**d**) After methane adsorption in kerogen (89.2 MPa).

Figure 10c,d show the water density profiles before and after methane adsorption in the kerogen pore. At a low water content (11.10%), the water distribution in the kerogen pore is basically not affected by methane adsorption. Abundant high-energy sites for methane adsorption remain unoccupied on the kerogen surfaces. With the increase in water content, methane adsorption promotes the fusion of water clusters, and the water clusters on the pore walls aggregate to form a larger cluster structure. At the high water content (32.23%), methane adsorption reduces the peak densities and extends the peak widths of the water adsorption layers, indicating that methane adsorption inhibits the spread of water clusters along the kerogen surfaces and promotes the growth of water clusters in the vertical direction of kerogen surfaces.

Figure 11 shows the density profiles of methane and water in shale illite and kerogen nanopores. Compared with the methane adsorption layer, the water adsorption layer is closer to the illite pore walls, indicating that the affinity of illite surfaces to water is stronger than that to methane. In the illite pores, the methane adsorption layers are located between the water adsorption layers. As the water content increases, the effective pore space decreases and the number of methane adsorption layers decreases. At a low water content, the illite surfaces are not fully covered by water molecules and there is a gas–solid interaction between the methane and illite walls. At a high water content, methane molecules are adsorbed on the water adsorption layers due to the steric hindrance effect of water adsorption. Methane adsorption is governed by gas–liquid interaction.

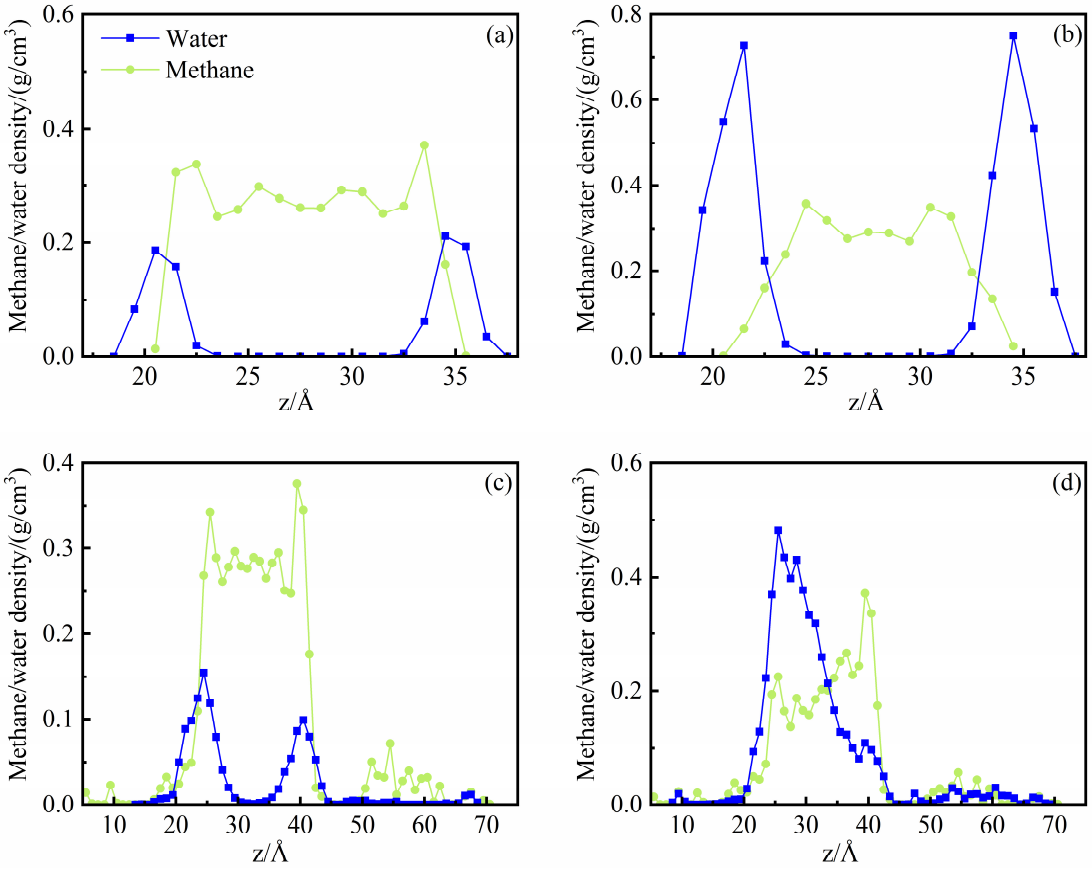

Figure 11. Density profiles of methane and water in shale nanopores (120 °C, 89.2 MPa): (**a**) Water content of 7.17% in illite; (**b**) Water content of 29.53% in illite; (**c**) Water content of 11.10% in kerogen; (**d**) Water content of 32.23% in kerogen.

Figure 11c,d shows that methane and water molecules are competitively adsorbed on the kerogen pore walls at a low water content, and methane molecules dominate in the intermolecular pores of the kerogen matrix. At a high water content, water clusters fuse on the kerogen pore walls. The peak density and peak width of the water adsorption layer on one side of the wall increase. Water clusters grow along the direction parallel to and perpendicular to the wall. Accordingly, the methane density in the water adsorption phase decreases. In addition to methane molecules, the intermolecular pores of the kerogen matrix contain numerous dissolved water molecules.

5. Conclusions

(1) Despite the discrepancies in methane adsorption capacity, the microscopic adsorption characteristics of methane in different mineral nanopores are basically consistent. At low pressure, methane is adsorbed in a monolayer form on the pore wall of each mineral. At high pressure, a concavo-convex transition zone forms close to the methane adsorption layer, complicating the correlation of the adsorption phase density with the excess adsorption amounts between minerals.

(2) Kerogen and illite slit pores do not differ significantly in terms of their intrinsic adsorption capacity for methane. The adsorption capacity per unit mass of kerogen is greater than that of illite due to the smaller molar mass of the kerogen skeleton and its large intermolecular porosity. The intermolecular pores of the kerogen matrix can accommodate part of the methane molecules in a dissolved state.

(3) In the illite pores, water molecules gradually occupy the high-energy adsorption sites of the pore wall and spread along the wall to form an adsorption layer. The affinity of the illite wall towards water is greater than that towards methane, and the methane

adsorption layers are between the water adsorption layers on the pore walls. Methane adsorption has little effect on water adsorption characteristics.

(4) In the kerogen pores, water molecules are preferentially aggregated on the polar functional groups to form clusters. At a high water content, methane adsorption can promote the fusion of the water clusters and inhibit the spread of the water clusters along the wall. Part of the water molecules can be dissolved in the kerogen matrix.

Author Contributions: Conceptualization, J.W., X.Y. and L.H.; methodology, S.H.; validation, S.Z., D.Z. and J.Z.; formal analysis, C.R. and C.Z.; investigation, J.W. and X.Y.; resources, R.J.; data curation, D.L.; writing—original draft preparation, J.W., X.Y., S.H., C.R., C.Z. and Q.Y.; writing—review and editing, S.Z., D.Z., J.Z., R.J., D.L. and L.H.; visualization, Q.Y.; supervision, L.H.; project administration, L.H.; funding acquisition, L.H. All authors have read and agreed to the published version of the manuscript.

Funding: This research was funded by the National Natural Science Foundation of China, Grant Nos. 52204031, 41972137 and 42002157, the Natural Science Foundation of Sichuan Province, Grant No. 2023NSFSC0947, and the Open Fund of State Key Laboratory of Oil and Gas Reservoir Geology and Exploitation (Chengdu University of Technology), Grant No. PLC20210303.

Data Availability Statement: The data that support the findings of this study are available upon reasonable request.

Conflicts of Interest: The authors declare no conflict of interest.

References

1. Huang, S.; Ma, X.; Yang, H.; Wu, J.; Zhang, J.; Zhao, S.; Zhang, D.; Ren, C.; Huang, L. Experimental characterization and molecular modeling of kerogen in Silurian deep gas shale from southern Sichuan Basin, China. *Energy Rep.* **2022**, *8*, 1497–1507. [CrossRef]
2. Loucks, R.G.; Ruppel, S.C. Mississippian Barnett Shale: Lithofacies and depositional setting of a deep-water shale-gas succession in the Fort Worth Basin, Texas. *AAPG Bull.* **2007**, *91*, 579–601. [CrossRef]
3. Yasin, Q.; Sohail, G.M.; Liu, K.-Y.; Du, Q.-Z.; Boateng, C.D. Study on brittleness templates for shale gas reservoirs-A case study of Longmaxi shale in Sichuan Basin, southern China. *Pet. Sci.* **2021**, *18*, 1370–1389. [CrossRef]
4. Karamov, T.; White, V.; Idrisova, E.; Kozlova, E.; Burukhin, A.; Morkovkin, A.; Spasennykh, M. Alterations of carbonate mineral matrix and kerogen micro-structure in Domanik organic-rich shale during anhydrous pyrolysis. *Minerals* **2022**, *12*, 870. [CrossRef]
5. Godinho, J.R.A.; Ma, L.; Chai, Y.; Storm, M.; Burnett, T.L. Mineral precipitation in fractures and nanopores within shale imaged using time-lapse x-ray tomography. *Minerals* **2019**, *9*, 480. [CrossRef]
6. Chalmers, G.R.; Bustin, R.M.; Power, I.M. Characterization of gas shale pore systems by porosimetry, pycnometry, surface area, and field emission scanning electron microscopy/transmission electron microscopy image analyses: Examples from the Barnett, Woodford, Haynesville, Marcellus, and Doig units. *AAPG Bull.* **2012**, *96*, 1099–1119.
7. Kar, N.R.; Mani, D.; Mukherjee, S.; Dasgupta, S.; Puniya, M.K.; Kaushik, A.K.; Biswas, M.; Babu, E.V.S.S.K. Source rock properties and kerogen decomposition kinetics of Eocene shales from petroliferous Barmer basin, western Rajasthan, India. *J. Nat. Gas Sci. Eng.* **2022**, *100*, 104497. [CrossRef]
8. Curtis, J.B. Fractured shale-gas systems. *AAPG Bull.* **2002**, *86*, 1921–1938.
9. Mohd Aji, A.Q.M.; Mohshim, D.F.; Maulianda, B.; El-Raeis, K.A. Molecular simulation study on methane adsorption in amorphous shale structure. *Minerals* **2023**, *13*, 214. [CrossRef]
10. Turlapati, V.Y.; Prusty, B.K.; Pal, S.K.; Raja, E. Examining supercritical methane adsorption on nanoporous shales using constant and varying adsorbed phase density approaches. *Energy Fuels* **2023**, *37*, 2078–2090. [CrossRef]
11. Heller, R.; Zoback, M. Adsorption of methane and carbon dioxide on gas shale and pure mineral samples. *J. Unconv. Oil Gas Resour.* **2014**, *8*, 14–24. [CrossRef]
12. Tian, Y.; Yan, C.; Jin, Z. Characterization of methane excess and absolute adsorption in various clay nanopores from molecular simulation. *Sci. Rep.* **2017**, *7*, 12040. [CrossRef] [PubMed]
13. Onawole, A.T.; Nasser, M.S.; Hussein, I.A.; Al-Marri, M.J.; Aparicio, S. Theoretical studies of methane adsorption on Silica-Kaolinite interface for shale reservoir application. *Appl. Surf. Sci.* **2021**, *546*, 149164. [CrossRef]
14. Bakshi, T.; Vishal, V. A review on the role of organic matter in gas adsorption in shale. *Energy Fuels* **2021**, *35*, 15249–15264. [CrossRef]
15. Huang, L.; Ning, Z.; Wang, Q.; Zhang, W.; Cheng, Z.; Wu, X.; Qin, H. Effect of organic type and moisture on CO_2/CH_4 competitive adsorption in kerogen with implications for CO_2 sequestration and enhanced CH_4 recovery. *Appl. Energy* **2018**, *210*, 28–43. [CrossRef]
16. Josh, M.; Esteban, L.; Piane, C.D.; Sarout, J.; Dewhurst, D.; Clennell, M. Laboratory characterisation of shale properties. *J. Pet. Sci. Eng.* **2012**, *88*, 107–124. [CrossRef]

17. Diaz-Perez, A.; Cortes-Monroy, I.; Roegiers, J.C. The role of water/clay interaction in the shale characterization. *J. Pet. Sci. Eng.* **2007**, *58*, 83–98. [CrossRef]
18. Kadoura, A.; Nair, A.K.N.; Sun, S. Adsorption of carbon dioxide, methane, and their mixture by montmorillonite in the presence of water. *Microporous Mesoporous Mater.* **2016**, *225*, 331–341. [CrossRef]
19. Huang, L.; Zhou, W.; Xu, H.; Wang, L.; Zou, J.; Zhou, Q. Dynamic fluid states in organic-inorganic nanocomposite: Implications for shale gas recovery and CO_2 sequestration. *Chem. Eng. J.* **2021**, *411*, 128423. [CrossRef]
20. Ruppert, L.F.; Sakurovs, R.; Blach, T.P.; He, L.; Melnichenko, Y.B.; Mildner, D.F.R.; Alcantar-Lopez, L. A USANS/SANS study of the accessibility of pores in the Barnett Shale to methane and water. *Energy Fuels* **2013**, *27*, 772–779. [CrossRef]
21. Abdulelah, H.; Negash, B.M.; Keshavarz, A.; Hoteit, H.; Iglauer, S. Interfacial and wetting properties in shale/methane/water and shale/methane/surfactant systems at geological conditions. *Energy Fuels* **2022**, *36*, 10155–10166. [CrossRef]
22. Zhang, B.; Kang, J.; Kang, T. Effect of water on methane adsorption on the kaolinite (0 0 1) surface based on molecular simulations. *Appl. Surf. Sci.* **2018**, *439*, 792–800. [CrossRef]
23. Merkel, A.; Fink, R.; Littke, R. The role of pre-adsorbed water on methane sorption capacity of Bossier and Haynesville shales. *Int. J. Coal Geol.* **2015**, *147*, 1–8. [CrossRef]
24. Geatches, D.L.; Wilcox, J. Ab initio investigations of dioctahedral interlayer-deficient mica: Modelling 1 M polymorphs of illite found within gas shale. *Eur. J. Mineral.* **2014**, *26*, 127–144. [CrossRef]
25. Plimpton, S. Fast parallel algorithms for short-range molecular dynamics. *J. Comput. Phys.* **1995**, *117*, 1–19. [CrossRef]
26. Cygan, R.T.; Liang, J.J.; Kalinichev, A.G. Molecular models of hydroxide, oxyhydroxide, and clay phases and the development of a general force field. *J. Phys. Chem. B* **2004**, *108*, 1255–1266. [CrossRef]
27. Xiao, S.; Edwards, S.A.; Gräter, F. A new transferable forcefield for simulating the mechanics of $CaCO_3$ crystals. *J. Phys. Chem. C* **2011**, *115*, 20067–20075. [CrossRef]
28. Hagler, A.T.; Lifson, S.; Dauber, P. Consistent force field studies of intermolecular forces in hydrogen-bonded crystals. 2. A benchmark for the objective comparison of alternative force fields. *J. Am. Chem. Soc.* **1979**, *101*, 5122–5130. [CrossRef]
29. Martin, M.G.; Siepmann, J.I. Transferable potentials for phase equilibria. 1. United-atom description of n-alkanes. *J. Phys. Chem. B* **1998**, *102*, 2569–2577. [CrossRef]
30. Berendsen, H.J.C.; Grigera, J.R.; Straatsma, T.P. The missing term in effective pair potentials. *J. Phys. Chem.* **1987**, *91*, 6269–6271. [CrossRef]
31. Shelley, J.C.; Patey, G.N. Boundary condition effects in simulations of water confined between planar walls. *Mol. Phys.* **1996**, *88*, 385–398. [CrossRef]
32. Lorentz, H.A. Ueber die anwendung des satzes vom virial in der kinetischen theorie der gase. *Ann. Der Phys.* **1881**, *248*, 127–136. [CrossRef]
33. Nosé, S. A unified formulation of the constant temperature molecular dynamics methods. *J. Chem. Phys.* **1984**, *81*, 511–519. [CrossRef]
34. Gelb, L.D.; Gubbins, K.E. Pore size distributions in porous glasses: A computer simulation study. *Langmuir* **1999**, *15*, 305–308. [CrossRef]
35. Huang, L.; Chen, Q.; Wu, J.; Yang, Q.; Zhang, J.; Huang, S.; Zhou, W.; Zou, J. Molecular simulation of methane adsorption characteristics in illite nanopores of deep shale reservoirs. *J. Cent. South Univ. (Sci. Technol.)* **2022**, *53*, 3522–3531.